Bias Dependence of Non-Fourier Heat Spreading in GaN HEMTs

Yang Shen, *Graduate Student Member, IEEE*, Xue-Song Chen, *Member, IEEE*, Yu-Chao Hua, Han-Ling Li, Lan Wei, *Senior Member, IEEE*, and Bing-Yang Cao

***Abstract*— In this article, self-heating in gallium nitride (GaN) high-electron-mobility transistors (HEMTs) is studied by combining the technology computer-aided design (TCAD) and phonon Monte Carlo (MC) simulations. The simulation results indicate that the bias-dependent heat generation in the channel can have a remarkable impact on the thermal spreading process and the phonon ballistic effects simultaneously. Based on the two-heat-source model, we propose a two-thermal-conductivity model to predict the device junction temperature with the consideration of bias-dependent phonon transport in the HEMT. The proposed model is easy to be coupled with the finite-element method (FEM)-based thermal analysis without the need for time-consuming multiscale electrothermal simulations.**

***Index Terms*— Ballistic transport, electrothermal simulation, gallium nitride (GaN) high-electron-mobility transistor (HEMT), phonon Monte Carlo (MC) simulation.**

I. Introduction

GALLIUM nitride (GaN)-based high-electron-mobility transistors (HEMTs) are attractive for high-power amplifiers and high-frequency switching applications [1]. Due to the wide bandgap of GaN and the 2-D electron gas (2DEG) formed at the AlGaN/GaN heterojunction, GaN HEMTs can sustain a high voltage and exhibit an excellent electron mobility [2]. However, owing to the high power density, significant self-heating in GaN HEMTs can degrade the device performance and shorten the device lifetime [3], [4], [5]. To accurately predict the junction temperature, thereby developing effective thermal management strategies, it is important to clearly understand the heat generation and transport process in GaN HEMTs.

The heat in the HEMT is primarily generated on the top of the GaN buffer layer with a width of about a few hundred nanometers and dissipated through the GaN layer to the substrate [6], [7]. The thickness of the GaN layer usually ranges from 1 to 3 μm, and the thickness of the substrate can be larger than 100 μm. Compared with the total device length and thickness, the heat source area of the HEMT is very small [8]. When heat spreads from a small area to a much larger region, there is a significant thermal spreading resistance, which can dominate the thermal transport process within the HEMT [9]. In addition, the main heat carriers in GaN are phonons whose mean free paths (MFPs) are generally larger than 100 nm [10], [11], which are comparable with the thickness of the GaN layer and the width of the heat generation region. The frequent boundary and interface scattering can lead to a reduced thermal conductivity of the GaN thin films [12], and the quasi-ballistic transport when the heat source size is comparable with the phonon MFP can further increase the hotspot temperature [13], [14], [15].

Based on Fourier's law of heat conduction, the thermal spreading process has been studied extensively, including the cases with eccentric heat sources [16], interfacial thermal resistance [17], anisotropic- and temperature-dependent thermal conductivities [18], [19], and so on. Hua et al. [20] investigated the thermal spreading resistance in a ballistic-diffusive regime and demonstrated that the phonon ballistic effects could result in a dramatic increase in the thermal resistance compared with Fourier's law-based predictions. In addition, the results indicate that the strength of the phonon ballistic effects can be significantly related to the geometric size of the system and the width of the heating area. Recently, the effects of phonon dispersion and the heating scheme on the thermal resistance of devices have also been studied [21], [22].

However, most of these studies assume that the heat source has the same length as the gate, which is modeled as either a surface heat flux or a uniform volumetric heat source on the top of the GaN layer. Whereas being the result of Joule heating, the heat generation in the HEMT is highly bias-dependent [23], [24]. At different biases, the heat source distributions in the channel can be quite different, which can have a marked impact on the thermal spreading process and the strength of the phonon ballistic effects. This necessitates

Manuscript received 24 September 2022; revised 22 November 2022; accepted 5 December 2022. Date of publication 19 December 2022; date of current version 24 January 2023. This work was supported by the National Natural Science Foundation of China under Grant 51825601 and Grant U20A20301. The review of this article was arranged by Editor S. Graham. *(Corresponding author: Bing-Yang Cao.)*

Yang Shen, Han-Ling Li, and Bing-Yang Cao are with the Key Laboratory of Thermal Science and Power Engineering of Education of Ministry, Department of Engineering Mechanics, Tsinghua University, Beijing 100084, China (e-mail: sy980829@163.com; lihanling1994@163.com; caoby@tsinghua.edu.cn).

Xue-Song Chen and Lan Wei are with the Department of Electrical and Computer Engineering, University of Waterloo, Waterloo, ON N2L 3G1, Canada (e-mail: xschen08@gmail.com; lan.wei@uwaterloo.ca).

Yu-Chao Hua is with the LTEN Laboratory, Polytech Nantes, University of Nantes, UMR6607, F-44000 Nantes, France (e-mail: huayuchao19@163.com).

Color versions of one or more figures in this article are available at https://doi.org/10.1109/TED.2022.3227894.

Digital Object Identifier 10.1109/TED.2022.3227894

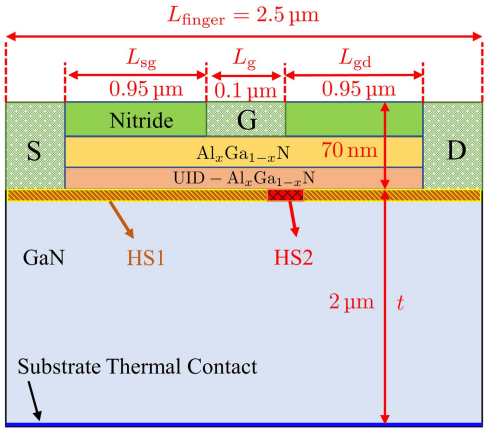

Fig. 1. Schematic of the GaN HEMT for TCAD simulations. S, G, and D refer to the source, gate, and drain, respectively.

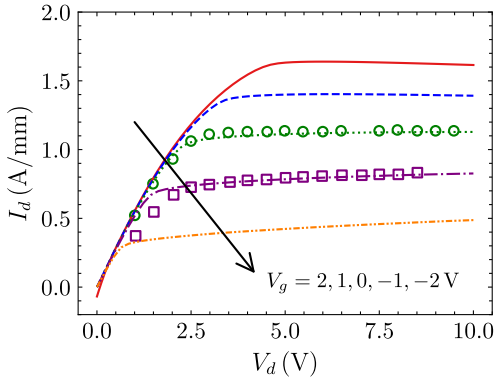

Fig. 2. Output characteristics of the HEMT from −2 to 2 V with an interval of 1 V extracted from TCAD simulations (lines) and experimental results (symbols) [30].

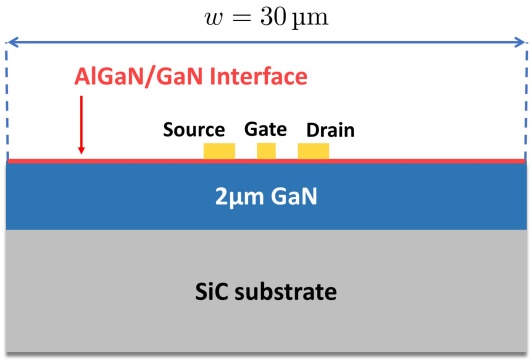

Fig. 3. Schematic of the GaN-on-SiC device for the phonon MC simulations; the TCAD simulation region is between the source and the drain. The geometries are not drawn to scale.

the examination of the influence of the bias-dependent heat generation on the thermal spreading process and phonon ballistic effects simultaneously. Though there has been some work on multiscale electrothermal simulations [25], [26], [27], [28], [29], indicating that the phonon ballistic effects can increase the device junction temperature compared with Fourier's law-based predictions, the quantitative analysis of bias-dependent phonon ballistic transport in GaN HEMTs has not been carried out.

In this work, we reexamine self-heating in GaN HEMTs by combining the technology computer-aided design (TCAD) and phonon Monte Carlo (MC) simulations. It is found that the bias-dependent heat generation in the channel can have a remarkable impact on the thermal spreading process and the phonon ballistic effects simultaneously. Based on the two-heat-source model, we propose a two-thermal-conductivity model that can easily reflect the influence of the bias-dependent non-Fourier heat spreading process on the device junction temperature without resorting to multiscale electrothermal simulations.

II. Simulation Methodology

A. TCAD Simulations

The GaN HEMT for TCAD simulations is shown in Fig. 1, which follows the structure of the device presented in [30]. From top to bottom, the layers are a 50-nm silicon nitride passivation layer, an 18-nm $Al_{0.25}Ga_{0.75}N$ layer with donor concentration $N_D = 2 \times 10^{18}$ cm^{-3}, a 2-nm unintentionally doped (UID) $Al_{0.25}Ga_{0.75}N$ spacer layer with donor concentration $N_D = 1 \times 10^{15}$ cm^{-3}, a 2-μm GaN buffer layer, and a 10-nm SiC substrate layer. The gate length is $L_g = 0.1$ μm, and the source and drain access regions have the same length of $L_{sg} = L_{gd} = 0.95$ μm. The total length of the activated region is $L_{\text{finger}} = 2.5$ μm.

Electrothermal TCAD simulations are conducted to predict the heat generation profiles at different biases, which are used to drive the phonon MC simulations. Since the focus of this work is the influence of bias-dependent heat generation on the thermal transport process, detailed electron–phonon interactions are not considered in this study [31]. The drift-diffusion model (DDM) is used for electron transport [32], which assumes that the electrons are in thermal equilibrium with the lattice. To consider the nonequilibrium energy transfer between electrons and phonons, electron MC simulations can be carried out to give the detailed phonon generation spectrum [33]. Fig. 2 shows the simulated output characteristics of the HEMT, which shows a good agreement with the experimental results.

B. Phonon MC Simulations

The phonon tracing MC simulation is an effective approach to simulate the ballistic-diffusive heat conduction, which can deal with the transport problems involving complex geometries, multiple interfaces, and arbitrary heat source distributions [34]. The detailed principles and procedures can be found in [35], [36], and [37]. Fig. 3 shows the schematic of the GaN-on-SiC device for the MC simulations, which is a typical structure for a period of multifinger GaN HEMT devices with a pinch distance $w = 30$ μm. The heat source only exists in the TCAD simulated region, which is in the center of the device between the source and the drain. Since the thin AlGaN layer has a very low thermal conductivity and the heat generation mainly exists in the GaN layer, the structures above the AlGaN/GaN interface are all neglected in the MC simulations [38]. The boundaries in the lateral

TABLE I
PHONON DISPERSION AND SCATTERING PARAMETERS

Parameter (Unit)	GaN	SiC
$k_0\,(1\times10^{9}\,\mathrm{m}^{-1})$	10.94	8.94
$\omega_m\,(1\times10^{13}\,\mathrm{rad/s})$	3.50	7.12
$a_D\,(\text{Å})$	2.87	3.51
$A\,(1\times10^{-45}\,\mathrm{s}^3)$	5.26	1.00
$B\,(1\times10^{-19}\,\mathrm{s/K})$	1.10	0.596
$C\,(\mathrm{K})$	200	235.0

direction are set as periodic, and the top boundary is adiabatic. Given that the heat conduction in the substrate is almost a 1-D process, the simulation thickness for the substrate in this work is only set as 30 μm, and the bottom is set as isothermal. For real device simulations, the bottom boundary condition can be easily changed to the nonuniform temperature distributions calculated using Fourier's law-based simulations [25], [26], [27], [28].

The phonon dispersion and relaxation time are needed to carry out the MC simulations. In this work, an isotropic sine-shaped phonon dispersion (Born–von Karman dispersion) is used for both GaN and SiC. In the dispersion model, the relation between the angular frequency ω and the wave vector k can be depicted as $\omega(k)=\omega_{\mathrm{m}}\sin(\pi k/2k_{\mathrm{m}})$, where $k_{\mathrm{m}}=(6\pi^2 n)^{1/3}$ with n as the volumetric density of primitive cells. The previous research has verified that this dispersion model can well reflect the phonon MFP spectrum of various materials [10]. The scattering mechanisms considered in this work include impurity scattering (I) and Umklapp scattering (U), and only point defects are included in the impurity scattering, since the previous work has indicated that these scattering mechanisms are the most essential ones in GaN [26], [39]. The relaxation time can be expressed as $\tau_{\mathrm{I}}^{-1}=A\omega^4$ and $\tau_{\mathrm{U}}^{-1}=B\omega^2 T\exp(-C/T)$, where A, B, and C are the fitting constants. The total relaxation time can be calculated using Matthiessen's rule $\tau^{-1}=\tau_{\mathrm{I}}^{-1}+\tau_{\mathrm{U}}^{-1}$ [40]. This work adopts the fit parameters in [26], as shown in Table I. The model calculated bulk thermal conductivities of GaN and SiC are 220 and 350 W/m.K, respectively, which is in agreement with the experimental values [41]. To better depict the phonon scattering process, more scattering mechanisms, such as dislocation scattering [42], grain boundary scattering [43], and normal phonon scattering [44], can be included based on the first-principle calculations in the future work.

To describe phonon transport in the GaN/SiC interface, the diffuse mismatch model (DMM) is used to calculate the interface phonon transmissivities [45]. In DMM, phonons are diffusively transmitted or reflected by an interface, and the phonon transmissivity with frequency ω from material 1 to 2 can be expressed as follows:

$$T_{12}(\omega)=\frac{\sum_p v_{2,g,p}(\omega)D_{2,p}(\omega)}{\sum_p v_{1,g,p}(\omega)D_{1,p}(\omega)+\sum_p v_{2,g,p}(\omega)D_{2,p}(\omega)} \tag{1}$$

where p is the phonon branch, $v_g(\omega)$ is the phonon group velocity, and $D(\omega)$ is the density of states. The thermal boundary resistance (TBR) of the GaN/SiC interface calculated using the MC simulations is 16 m^2 K/GW, which is in the same range as the experimental results (4 20m^2. K/GW) [46], [47], [48], [49]. The DMM only includes harmonic interfacial phonon–phonon scatterings and ignores the contribution of the harmonic interactions [50]. The full-band phonon dispersion and interfacial transmissivities are expected to be incorporated in the phonon MC simulations to simulate the near-junction thermal transport process more accurately [51], [52], [53].

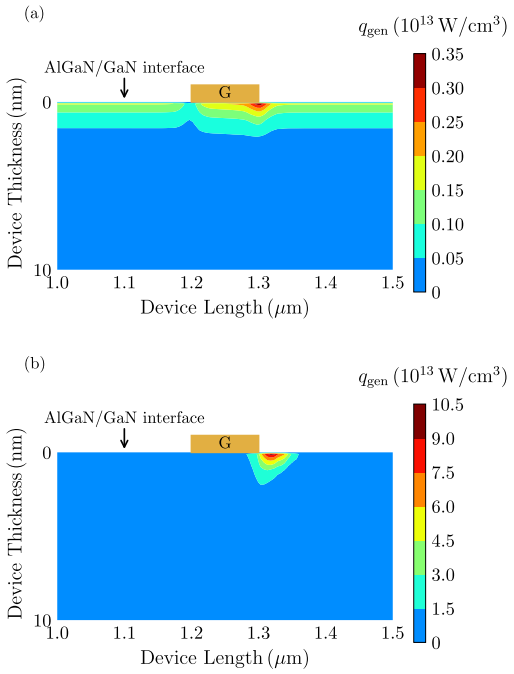

Fig. 4. Heat generation in the channel extracted from TCAD simulations at two biases (a) $V_g=2$ V, $V_d=3.8$ V and (b) $V_g=-1$ V, $V_d=6.7$ V with an identical power dissipation $P_{\mathrm{diss}}=5$ W/mm.

III. RESULTS AND DISCUSSION

A. Bias-Dependent Heat Generation

Fig. 4 shows the heat generation profiles in the channel at two biases with an identical power dissipation $P_{\mathrm{diss}}=5$ W/mm extracted from TCAD simulations. The heat generation mainly exists within a 2-nm region below the AlGaN/GaN interface and is highly bias-dependent. At $V_g=2$ V, the heat spans relatively uniformly in the whole channel. Whereas for the condition at $V_g=-1$ V, the heat is concentrated at the drain-side gate edge with a much larger heat density.

To represent the bias-dependent heat generation caused by the nonuniform electric field in the channel, Chen et al. [32] proposed a two-heat-source model, which divided the total heat dissipation into two parts, as shown in Fig. 1. Heat Source 1 (HS1) spanning the whole finger length (L_{finger}) represents the relatively low and uniform heat generation in the channel. Heat Source 2 (HS2) centered at the drain-side gate edge represents the concentrated heat generation under the high electric field. The length of HS1 (L_{HS1}) is the same as the finger length, and the length of HS2 (L_{HS2}) is set as 0.16 μm to approximate the length of the high-field region. L_{HS2} is independent of the bias and device geometry, since the width of the high-field region nearly does not change with these parameters [23], [24], [32]. When the device is

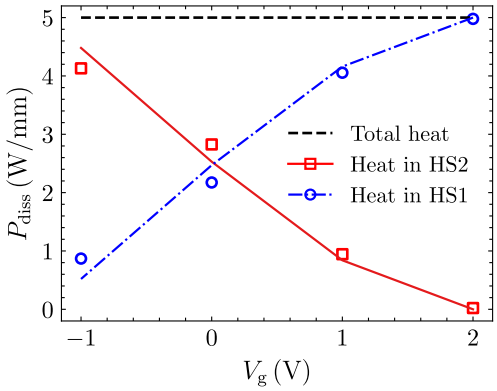

Fig. 5. Heat dissipation in HS1 and HS2 with an identical power dissipation $P_{\rm diss} = 5$ W/mm predicted by the two-heat-source model (lines) and extracted from TCAD simulations (symbols). The four bias points are $(V_g, V_d) = (-1\ \text{V}, 6.7\ \text{V})$, (0 V, 5 V), (1 V, 4.1 V), and (2 V, 3.8 V).

in the linear regime, i.e., V_d is less than the drain saturation voltage $V_{\rm dsat}$, all the heat is dissipated in HS1. As the channel is pinched-off and the device works in the saturation regime, i.e., $V_d > V_{\rm dsat}$, the heat dissipated in HS1 stays the maximum, and the excessive heat is only dissipated in HS2. The model can be expressed as follows:

$$\begin{cases} P_1 = I_d V_d,\ P_2 = 0, & V_d \le V_{\rm dsat} \\ P_1 = I_d V_{\rm dsat},\ P_2 = I_d (V_d - V_{\rm dsat}), & V_d > V_{\rm dsat} \end{cases} \tag{2}$$

where P_1 and P_2 are the power dissipations in HS1 and HS2, respectively. Fig. 5 shows the power dissipated in the two heat sources predicted by (2) and extracted from TCAD simulations at $P_{\rm diss} = 5$ W/mm. A good agreement is achieved at different biases. Also, it can be found that at the same power dissipation, more heat is dissipated in HS2 for the bias with a lower V_g, since the device has to work deeper to maintain the same $P_{\rm diss}$.

B. Temperature Distribution in the HEMT

Fig. 6 shows the temperature rise distributions relative to the heat sink in the GaN layer predicted by the MC simulations at two biases with an identical power dissipation $P_{\rm diss} = 5$ W/mm. At $V_g = 2$V, the maximum temperature rise is around 70 K. Whereas at $V_g = -1$V, the maximum temperature rise can reach about 300 K. The results can be explained by Fig. 5; at $V_g = 2$V, the heat is almost dissipated in HS1. Whereas at $V_g = -1$V, most heat is dissipated in HS2 with a much smaller size. The decrease of the heat source size can result in a much larger thermal spreading resistance and the ballistic effect with the heat source size comparable with MFP. Also, it is revealed by the comparison that the ballistic effect can significantly change the temperature profiles. As the size of the heat source decreases, the lack of internal phonon scatterings can cause the temperatures to decay more rapidly away from the hot area. At $V_g = 2$V, the temperature change in the whole GaN layer is less than 60 K, whereas at $V_g = -1$V, the temperature drops by nearly 200 K in a 50-nm range along thickness.

Fig. 7 compares the temperature rise distributions at the drain-side gate edge along thickness predicted by the MC

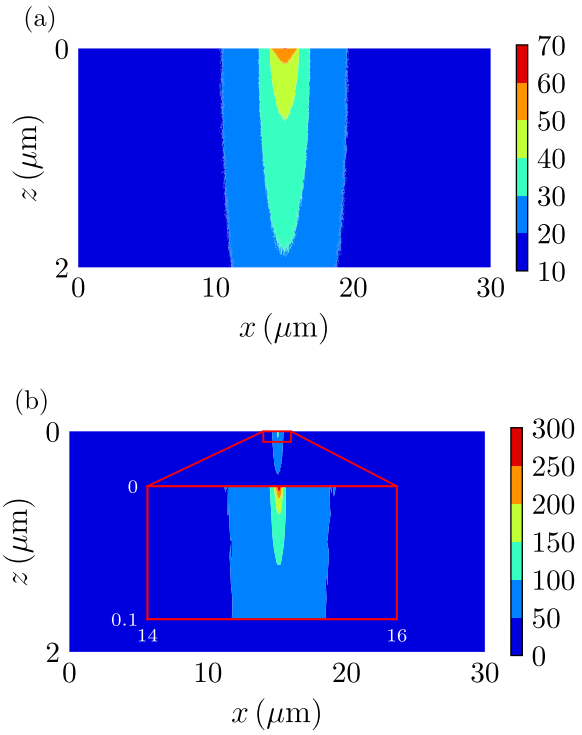

Fig. 6. Temperature rise distributions in the GaN layer at different biases (a) $V_g = 2$ V, $V_d = 3.8$ V and (b) $V_g = -1$ V, $V_d = 6.7$ V predicted by the MC simulations with an identical power dissipation $P_{\rm diss} = 5$ W/mm.

simulations at the two biases. The results predicted by the finite-element method (FEM) with the bulk thermal conductivities are also given for comparison. Compared with the FEM results, the temperatures predicted by the MC simulations are much higher in the hotspot region due to the strong phonon ballistic effects. As the distance away from the hotspot increases, the MC simulation temperatures gradually become consistent with the FEM results, since the phonon scattering enhances, and the heat starts to transport in a diffusive way. In addition, it more clearly shows that the size of the heat source can have a remarkable influence on the hotspot temperature distributions. At the bias with a lower V_g, the heat source size-induced ballistic effect can significantly increase the maximum temperature and decays rapidly away from the hotspot.

The channel temperature profiles predicted by the MC simulations and FEM at the two biases are also plotted in Fig. 8. It can be found that due to the different heat generation profiles, the temperature distributions exhibit a very distinct behavior. At $V_g = 2$ V, the heat spans relatively uniformly in HS1 with a low heat density. In this case, the temperature distributions in the heat source region are smooth, and the difference between the MC simulations and FEM is not too significant due to the relatively weak phonon ballistic effect. Whereas at $V_g = -1$ V, the heat generation is highly concentrated in HS2 with a small size, and the strong phonon ballistic effect leads to a dramatic increase in the hotspot temperature. The same phenomenon can also be observed from the experimental results [28].

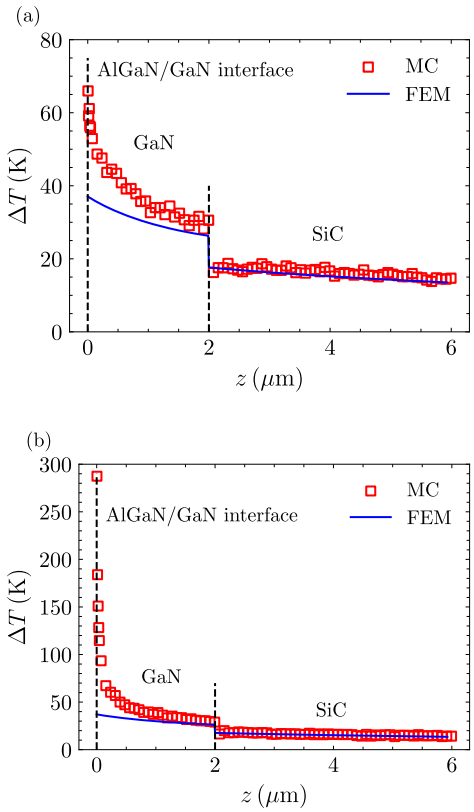

Fig. 7. Comparison of the temperature rise distributions through the depth of the HEMT at drain-side gate edge (a) $V_g = 2$ V, $V_d = 3.8$ V and (b) $V_g = -1$ V, $V_d = 6.7$ V with an identical power dissipation $P_{\text{diss}} = 5$ W/mm computed by the MC simulations and FEM.

C. Thermal Resistance of the GaN Layer

As shown in Fig. 7, since the heat transports nearly diffusively away from the heat source, this work mainly focuses on analyzing the bias dependence of the thermal resistance of the GaN layer. Fig. 9 shows the temperature rise in the GaN layer ΔT_{GaN} as a function of the power dissipation P_{diss} extracted from the MC simulations and FEM at the two biases. To reduce the statistical uncertainty and moderate the influence of the nonlocal electron transport in a peaked electric region [26], [54], the maximum temperature defined in this work is the average temperature of HS2. As shown in Fig. 9, for both biases, the curve of ΔT_{GaN} against P_{diss} can be divided into two parts. When the device works in the linear regime, ΔT_{GaN} increases with P_{diss} slowly, and the MC simulation temperatures are only moderately higher than the FEM results, since in this regime, the heat is mainly dissipated in HS1 with a relatively large width. When the device is pinched-off and works in the saturation regime, ΔT_{GaN} increases with P_{diss} rapidly, and the MC simulation-predicted temperatures are much higher than the FEM predictions, since the heat starts to be concentrated in HS2 with a much smaller size, and the phonon ballistic effect is significantly enhanced.

To better reveal the bias dependence of the phonon ballistic effects, the differential thermal resistance of the GaN layer R_{diff} varying with the power dissipation P_{diss} can be computed. R_{diff} is defined as the derivative of ΔT_{GaN} versus P_{diss}, which is the slope of the curves plotted in Fig. 9. Fig. 10(a) shows

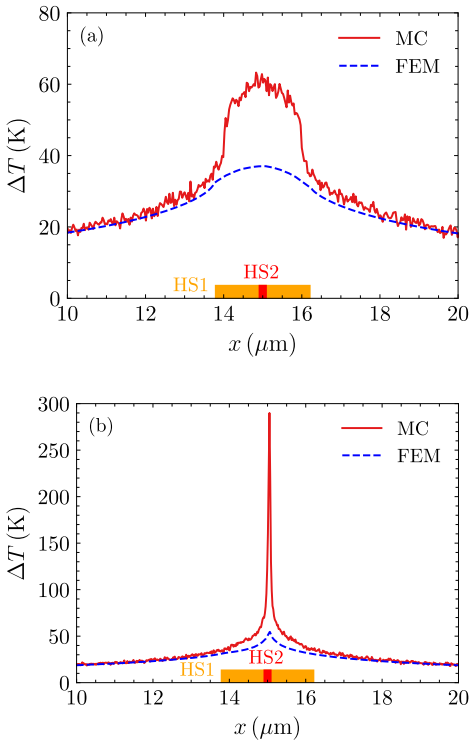

Fig. 8. Comparison of the channel temperature profiles at two biases (a) $V_g = 2$V, $V_d = 3.8$ V and (b) $V_g = -1$ V, $V_d = 6.7$ V with an identical power dissipation $P_{\text{diss}} = 5$ W/mm.

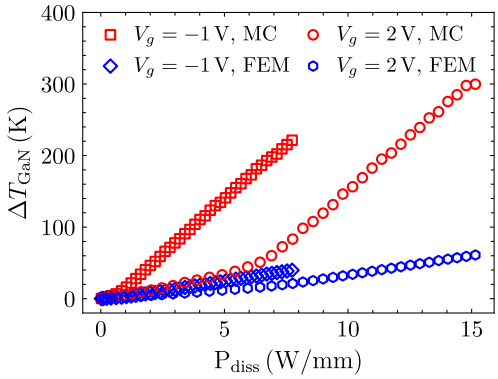

Fig. 9. Comparison of the temperature rise of the GaN layer as a function of P_{diss} with between the MC simulations and the FEM at different biases.

the FEM-predicted R_{diff} as a function of P_{diss}. At any gate voltage, R_{diff} stays low and nearly constant with P_{diss} in the linear regime, increases rapidly when the device enters the saturation regime, and reaches the same plateau value finally. This indicates that with the decrease in the heat source size, the thermal spreading effect alone can have a strong bias dependence. The MC simulation results shown in Fig. 10(b) exhibit a similar P_{diss}-dependent behavior of R_{diff}. In both regimes, the MC simulation-predicted R_{diff} is much higher than the FEM results, and the deviations are more significant in the saturation regime due to the enhanced phonon ballistic effect with the decreased size of the heat source.

As indicated in [20], three effects can affect the thermal transport in the GaN layer: 1) the thermal spreading effect associated with the system shape and the size of the heat

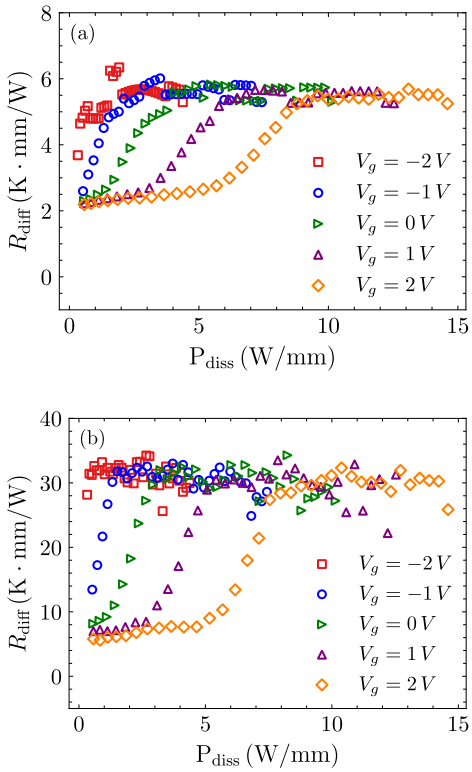

Fig. 10. Differential thermal resistance of the GaN layer R_{diff}, computed as the derivative of ΔT_{GaN} versus P_{diss} predicted by (a) FEM and (b) MC simulations.

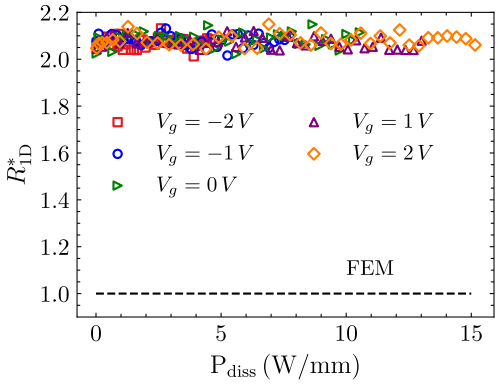

Fig. 11. Dimensionless 1-D thermal resistance of the GaN layer R^*_{1D} varying with P_{diss} computed by the MC simulations.

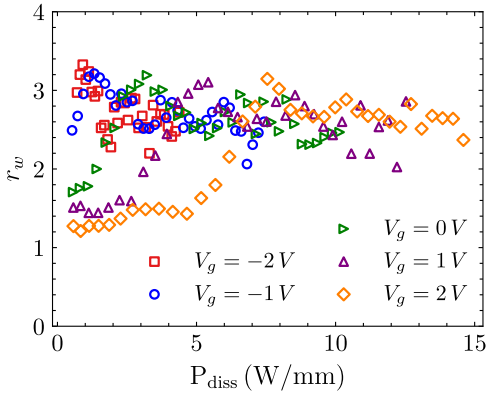

Fig. 12. Thermal resistance ratio r_w as a function of power dissipation P_{diss} at different biases.

source; 2) the cross-plane ballistic effect controlled by the film thickness; and 3) the ballistic effect with the heat source size comparable with MFP. To figure out the bias dependence of the non-Fourier heat spreading process in the HEMT, the key issue here is to separate the impacts of different mechanisms. First, we focus on the influence of the cross-plane ballistic effect on thermal resistance. A dimensionless 1-D thermal resistance R^*_{1D} can be defined to eliminate the impacts of the thermal spreading effect and the ballistic effect with the heat source size comparable with MFP

$$R^*_{\text{1D}} = \frac{R_{\text{1D}}}{R_{\text{1D\_0}}} \tag{3}$$

where R_{1D} is the 1-D thermal resistance calculated using the average temperature of the top and bottom of the GaN layer. $R_{\text{1D\_0}}$ is the 1-D thermal resistance calculated using the bulk thermal conductivity, $R_{\text{1D\_0}} = t/(wk_0)$, where w and t are the width and thickness of the GaN layer, respectively.

As shown in Fig. 11, R^*_{1D} extracted from the MC simulations is always approximately twice the FEM results at different biases. It is because the cross-plane ballistic effect is only related to the film thickness, which can be represented by using a thickness-dependent thermal conductivity of GaN films [38]. However, it should be noted that the temperatures predicted by the FEM using the thermal conductivity of GaN films are slightly lower than the MC simulation results, since the phonon-boundary scattering is enhanced with the internal heat source compared with the film in contact with two heat sinks with different temperatures [55].

To evaluate the heat source size-induced ballistic effect, a thermal resistance ratio r_w can be defined as follows:

$$r_w = R_{\text{diff, MC}}/\left(R_{\text{diff, FEM}} \cdot R^*_{\text{1D, MC}}\right) \tag{4}$$

where $R_{\text{diff, MC}}$ and $R_{\text{diff, FEM}}$ are the differential thermal resistance R_{diff} computed by the MC simulations and FEM, respectively. $R^*_{\text{1D, MC}}$ is the dimensionless 1-D thermal resistance of the GaN layer calculated by the MC simulations. The influences of the thermal spreading effect and the cross-plane ballistic effect are eliminated in $R_{\text{diff, FEM}}$ and $R^*_{\text{1D, MC}}$, respectively.

Fig. 12 shows r_w varying with P_{diss} at different biases, which shows a similar pattern as Fig. 10. In the linear regime, r_w is only slightly larger than 1, and the difference between the MC simulations and FEM is dominated by the cross-plane ballistic effect. However, when the device enters the saturation regime, r_w increases rapidly and reaches a plateau value, since the concentrated heat generation leads to a significant increase in the ballistic effect with heat source size comparable with MFP.

D. Two-Thermal-Conductivity Model

Based on phonon Boltzmann transport equation (BTE) and MC simulations, the previous work has established an effective thermal conductivity model for the thermal spreading process

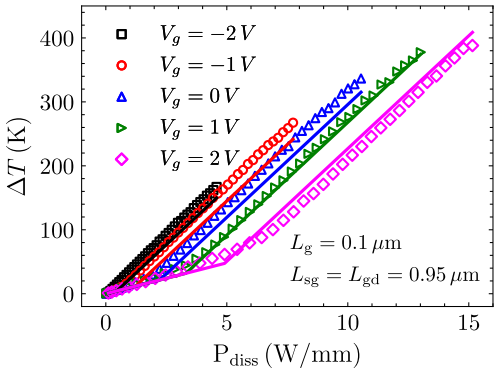

Fig. 13. Maximum temperature rise of the HEMT as a function of total power dissipation P_{diss} at different biases. The symbols are extracted from the MC simulations, and the lines are computed using the two-thermal-conductivity model based on the FEM results.

in a ballistic-diffusive regime [20], [21], [22]

$$k_{\text{eff}} = \frac{1}{3}\sum_j \int_0^{\omega_j} \hbar\omega \frac{\partial f_0}{\partial T}\,\text{DOS}_j(\omega) v_{g,\omega,j} l_{m,j}\,\text{d}\omega \tag{5}$$

where

$$l_{m,j} = \frac{l_{0,j}}{\left(1+\frac{2}{3}Kn_{t\_\omega,j}\right)\left(1+A_w\left(\frac{w_g}{w},\frac{w}{t}\right)Kn_{w\_\omega,j}\right) r_t r_{wg}} \tag{6}$$

in which $l_{0,j}$ is the intrinsic frequency-dependent MFP of the j branch phonon. $Kn_{t\_\omega,j} = l_{0,j}/t$ and $Kn_{w\_\omega,j} = l_{0,j}/w_g$ are the phonon branch-dependent Knudsen numbers, where t and w_g are the thickness of the GaN layer and the width of the heat generation region, respectively. In the model, $1 + 2/3Kn_{t\_\omega,j}$ corresponds to the cross-plane ballistic effect, and $1 + A_w Kn_{w\_\omega,j}$ represents the ballistic effect with heat source size comparable with MFP, where A_w is a fit parameter related to w/t and w_g/w. r_t and r_{wg} are the coefficients to reflect the influence of the phonon dispersion. When the material or the geometric parameters, such as t and w_g, change, the model can predict a different effective thermal conductivity to reflect the variation of the strength of the phonon ballistic effects. The model provides an easy approach to consider the influence of the ballistic effects in thermal spreading process and has been validated for different situations [21]. Using the model-predicted effective thermal conductivity, Fourier's law-based predictions can give the junction temperature close to simulation results based on phonon BTE [21]. The detailed discussions of the model can be found in [20], [21], and [22].

In the two-heat-source model, the heat generation regions in the channel are divided into HS1 and HS2, whose widths are $L_{\text{HS1}} = L_{\text{finger}}$ and $L_{\text{HS2}} = 0.16\ \mu$m, respectively. The effective thermal conductivities corresponding to HS1 and HS2 can be easily evaluated using the effective thermal conductivity model. For the phonon properties and geometric parameters adopted in this work, the k_{eff} values of HS1 and HS2 are $k_{\text{HS1}} = 94.47$ W/m.K and $k_{\text{HS2}} = 47.38$ W/m.K, respectively. The junction temperature of the GaN HEMT can then be computed by combining the two-heat-source model and the

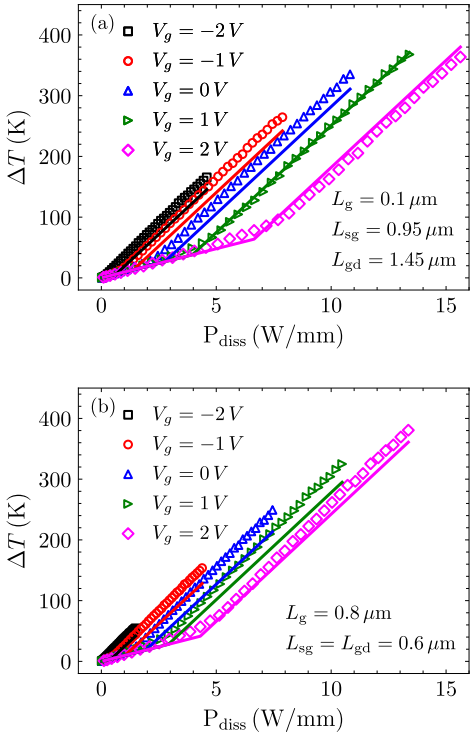

Fig. 14. Comparison of the maximum temperature rise of the HEMT versus total power dissipation P_{diss} at different biases for two more devices. (a) $L_g = 0.1\ \mu$m, $L_{sg} = 0.95\ \mu$m, and $L_{gd} = 1.45\ \mu$m. (b) $L_g = 0.8\ \mu$m and $L_{sg} = L_{gd} = 0.6\ \mu$m. The symbols are extracted from the MC simulations, and the lines are computed using the two-thermal-conductivity model based on the FEM results.

two-thermal-conductivity model

$$T_{\text{m}} = T_0 + \frac{k_{\text{bulk}}}{k_{\text{HS1}}} P_1 R_1 + \frac{k_{\text{bulk}}}{k_{\text{HS2}}} P_2 R_2 \tag{7}$$

where T_0 is the highest temperature at the bottom of the GaN layer calculated by the FEM, and R_1 and R_2 are the thermal resistances corresponding to HS1 and HS2 of the GaN layer, respectively. It should be noted that since the heat transport in the HEMT is not a 1-D process, the above thermal resistance model is just an approximation to reflect the influence of the ballistic effects on the thermal resistance of the GaN HEMT.

Fig. 13 shows the overall temperature rise of the HEMT at different biases calculated by the MC simulations and the model based on the FEM results; a good agreement is achieved at different biases and power dissipations. Devices with different geometries are also simulated to validate the model's applicability. Fig. 14 shows the results of the devices with [Fig. 14(a)] a longer drain access region and [Fig. 14(b)] a longer gate length, which also show good consistency at different biases.

IV. Conclusion

In this work, the non-Fourier heat spreading process in GaN HEMTs is studied by combining the TCAD and phonon MC simulations. The simulation results indicate that the bias-dependent heat generation in the channel can significantly affect the thermal spreading process and the phonon ballistic effects simultaneously. Based on the two-heat-source model,

this work presents a two-thermal-conductivity model, which can be easily incorporated with the FEM-based thermal analysis to reflect bias-dependent phonon ballistic transport in GaN HEMTs. The higher thermal conductivity reflects the weak ballistic effect when the channel has a relatively uniform heat distribution in the linear regime, and the lower one reflects the strong ballistic effect caused by the concentrated heat generation in the high-field region in the saturation regime. The model provides a simple approach to predict the junction temperature of the HEMT without resorting to multiscale electrothermal simulations.

REFERENCES

[1] K. Hirama, M. Kasu, and Y. Taniyasu, "RF high-power operation of AlGaN/GaN HEMTs epitaxially grown on diamond," *IEEE Electron Device Lett.*, vol. 33, no. 4, pp. 513–515, Apr. 2012.

[2] U. K. Mishra, P. Parikh, and Y.-F. Wu, "AlGaN/GaN HEMTs—An overview of device operation and applications," *Proc. IEEE*, vol. 90, no. 6, pp. 1022–1031, Jun. 2002.

[3] K. Ranjan, S. Arulkumaran, G. I. Ng, and A. Sandupatla, "Investigation of self-heating effect on DC and RF performances in AlGaN/GaN HEMTs on CVD-diamond," *IEEE J. Electron Devices Soc.*, vol. 7, pp. 1264–1269, 2019.

[4] M. Rosker et al., "The DARPA wide band gap semiconductors for RF applications (WBGS-RF) program: Phase II results," *CS ManTech*, vol. 1, pp. 1–4, May 2009.

[5] Y.-R. Wu and J. Singh, "Transient study of self-heating effects in AlGaN/GaN HFETs: Consequence of carrier velocities, temperature, and device performance," *J. Appl. Phys.*, vol. 101, Jun. 2007, Art. no. 113712.

[6] E. R. Heller and A. Crespo, "Electro-thermal modeling of multifinger AlGaN/GaN HEMT device operation including thermal substrate effects," *Microelectron. Rel.*, vol. 48, no. 1, pp. 45–50, Jan. 2008.

[7] J. Cho, Z. Li, M. Asheghi, and K. E. Goodson, "Near-junction thermal management: Thermal conduction in gallium nitride composite substrates," *Annu. Rev. Heat Transf.*, vol. 18, pp. 7–45, Jan. 2015.

[8] K. R. Bagnall, Y. S. Muzychka, and E. N. Wang, "Analytical solution for temperature rise in complex multilayer structures with discrete heat sources," *IEEE Trans. Compon., Packag., Manuf. Technol.*, vol. 4, no. 5, pp. 817–830, May 2014.

[9] M. Razavi, Y. S. Muzychka, and S. Kocabiyik, "Review of advances in thermal spreading resistance problems," *J. Thermophys. Heat Transf.*, vol. 30, no. 4, pp. 863–879, Oct. 2016.

[10] J. P. Freedman, J. H. Leach, E. A. Preble, Z. Sitar, R. F. Davis, and J. A. Malen, "Universal phonon mean free path spectra in crystalline semiconductors at high temperature," *Sci. Rep.*, vol. 3, no. 1, pp. 1–6, Dec. 2013.

[11] D.-S. Tang, G.-Z. Qin, M. Hu, and B.-Y. Cao, "Thermal transport properties of GaN with biaxial strain and electron-phonon coupling," *J. Appl. Phys.*, vol. 127, no. 3, Jan. 2020, Art. no. 035102.

[12] D. G. Cahill et al., "Nanoscale thermal transport. II. 2003–2012," *Appl. Phys. Rev.*, vol. 1, no. 1, p. 011305, 2014.

[13] Y. Hu, L. Zeng, A. J. Minnich, M. S. Dresselhaus, and G. Chen, "Spectral mapping of thermal conductivity through nanoscale ballistic transport," *Nature Nanotechnol.*, vol. 10, pp. 701–706, Jun. 2015.

[14] L. Zeng et al., "Measuring phonon mean free path distributions by probing quasiballistic phonon transport in grating nanostructures," *Sci. Rep.*, vol. 5, no. 1, pp. 1–10, 2015.

[15] G. Chen, "Non-Fourier phonon heat conduction at the microscale and nanoscale," *Nature Rev. Phys.*, vol. 3, no. 8, pp. 555–569, 2021.

[16] Y. S. Muzychka, J. R. Culham, and M. M. Yovanovich, "Thermal spreading resistance of eccentric heat sources on rectangular flux channels," *J. Electron. Packag.*, vol. 125, no. 2, pp. 178–185, 2003.

[17] Y. S. Muzychka, K. R. Bagnall, and E. N. Wang, "Thermal spreading resistance and heat source temperature in compound orthotropic systems with interfacial resistance," *IEEE Trans. Compon., Packag., Manuf. Technol.*, vol. 3, no. 11, pp. 1826–1841, Nov. 2013.

[18] A. Gholami and M. Bahrami, "Thermal spreading resistance inside anisotropic plates with arbitrarily located hotspots," *J. Thermophys. Heat Transf.*, vol. 28, no. 4, pp. 679–686, Aug. 2014.

[19] A. Darwish, A. J. Bayba, and H. A. Hung, "Channel temperature analysis of GaN HEMTs with nonlinear thermal conductivity," *IEEE Trans. Electron Devices*, vol. 62, no. 3, pp. 840–846, Mar. 2015.

[20] Y.-C. Hua, H.-L. Li, and B.-Y. Cao, "Thermal spreading resistance in ballistic-diffusive regime for GaN HEMTs," *IEEE Trans. Electron Devices*, vol. 66, no. 8, pp. 3296–3301, Aug. 2019.

[21] Y. Shen, Y.-C. Hua, H.-L. Li, S. L. Sobolev, and B.-Y. Cao, "Spectral thermal spreading resistance of wide-bandgap semiconductors in ballistic-diffusive regime," *IEEE Trans. Electron Devices*, vol. 69, no. 6, pp. 3047–3054, Jun. 2022.

[22] H.-L. Li, Y. Shen, Y.-C. Hua, S. L. Sobolev, and B.-Y. Cao, "Hybrid Monte Carlo-diffusion studies of modeling self-heating in ballistic-diffusive regime for gallium nitride HEMTs," *J. Electron. Packag.*, vol. 145, no. 1, Mar. 2022.

[23] X. Chen, S. Boumaiza, and L. Wei, "Self-heating and equivalent channel temperature in short gate length GaN HEMTs," *IEEE Trans. Electron Devices*, vol. 66, no. 9, pp. 3748–3755, Sep. 2019.

[24] O. Odabasi, M. O. Akar, B. Butun, and E. Ozbay, "Improved T_{MAX} estimation in GaN HEMTs using an equivalent hot point approximation," *IEEE Trans. Electron Devices*, vol. 67, no. 4, pp. 1553–1559, Apr. 2020.

[25] N. Donmezer and S. Graham, "The impact of noncontinuum thermal transport on the temperature of AlGaN/GaN HFETs," *IEEE Trans. Electron Devices*, vol. 61, no. 6, pp. 2041–2048, Jun. 2014.

[26] Q. Hao, H. Zhao, and Y. Xiao, "A hybrid simulation technique for electrothermal studies of two-dimensional GaN-on-SiC high electron mobility transistors," *J. Appl. Phys.*, vol. 121, no. 20, p. 204501, 2017.

[27] Q. Hao, H. Zhao, Y. Xiao, Q. Wang, and X. Wang, "Hybrid electrothermal simulation of a 3-D fin-shaped field-effect transistor based on GaN nanowires," *IEEE Trans. Electron Devices*, vol. 65, no. 3, pp. 921–927, Mar. 2018.

[28] B. Chatterjee et al., "Nanoscale electro-thermal interactions in AlGaN/GaN high electron mobility transistors," *J. Appl. Phys.*, vol. 127, no. 4, Jan. 2020, Art. no. 044502.

[29] H. Rezgui et al., "Design optimization of nanoscale electrothermal transport in 10 nm SOI FinFET technology node," *J. Phys. D, Appl. Phys.*, vol. 53, no. 49, Sep. 2020, Art. no. 495103.

[30] W. Jatal, U. Baumann, K. Tonisch, F. Schwierz, and J. Pezoldt, "High-frequency performance of GaN high-electron mobility transistors on 3C-SiC/Si substrates with Au-free ohmic contacts," *IEEE Electron Device Lett.*, vol. 36, no. 2, pp. 123–125, Feb. 2014.

[31] E. Pop, S. Sinha, and K. E. Goodson, "Heat generation and transport in nanometer-scale transistors," *Proc. IEEE*, vol. 94, no. 8, pp. 1587–1601, Aug. 2006.

[32] X. Chen, S. Boumaiza, and L. Wei, "Modeling bias dependence of self-heating in GaN HEMTs using two heat sources," *IEEE Trans. Electron Devices*, vol. 67, no. 8, pp. 3082–3087, Aug. 2020.

[33] E. Pop, "Monte Carlo transport and heat generation in semiconductors," *Annu. Rev. Heat Transf.*, vol. 17, pp. 385–423, Jan. 2014.

[34] H. Bao, J. Chen, X. Gu, and B.-Y. Cao, "A review of simulation methods in micro/nanoscale heat conduction," *ES Energy Environ.*, vol. 1, pp. 16–55, Sep. 2018.

[35] J.-P. M. Péraud and N. G. Hadjiconstantinou, "An alternative approach to efficient simulation of micro/nanoscale phonon transport," *Appl. Phys. Lett.*, vol. 101, no. 15, Oct. 2012, Art. no. 153114.

[36] H.-L. Li, J. Shiomi, and B.-Y. Cao, "Ballistic-diffusive heat conduction in thin films by phonon Monte Carlo method: Gray medium approximation versus phonon dispersion," *J. Heat Transf.*, vol. 142, no. 11, Nov. 2020, Art. no. 112502.

[37] X. Ran and M. Wang, "A steady-state energy-based Monte Carlo method for phonon transport with arbitrary temperature difference," *J. Heat Transf.*, vol. 144, no. 8, Aug. 2022, Art. no. 082502.

[38] C. Song, J. Kim, and J. Cho, "The effect of GaN epilayer thickness on the near-junction thermal resistance of GaN-on-diamond devices," *Int. J. Heat Mass Transf.*, vol. 158, Sep. 2020, Art. no. 119992.

[39] B. A. Danilchenko, I. A. Obukhov, T. Paszkiewicz, S. Wolski, and A. Jeżowski, "On the upper limit of thermal conductivity GaN crystals," *Solid State Commun.*, vol. 144, nos. 3–4, pp. 114–117, Oct. 2007.

[40] G. Chen, *Nanoscale Energy Transport and Conversion: A Parallel Treatment of Electrons, Molecules, Phonons, and Photons*. Oxford, U.K.: Oxford Univ. Press, 2005.

[41] Q. Hao, H. Zhao, and Y. Xiao, "Multi-length scale thermal simulations of GaN-on-SiC high electron mobility transistors," in *Multiscale Thermal Transport in Energy Systems*, Y. Zhang and Y.-L. He, Eds. Hauppauge, NY, USA: Nova, 2016.

[42] Y. Sun, Y. Zhou, M. Hu, G. J. Snyder, B. Xu, and W. Liu, "Probing the phonon mean free paths in dislocation core by molecular dynamics simulation," *J. Appl. Phys.*, vol. 129, no. 5, Feb. 2021, Art. no. 055103.

[43] Y. Zhou, X. Gong, B. Xu, and M. Hu, "Decouple electronic and phononic transport in nanotwinned structures: A new strategy for enhancing the figure-of-merit of thermoelectrics," *Nanoscale*, vol. 9, no. 28, pp. 9987–9996, 2017.

[44] F. X. Alvarez, D. Jou, and A. Sellitto, "Phonon hydrodynamics and phonon-boundary scattering in nanosystems," *J. Appl. Phys.*, vol. 105, no. 1, Jan. 2009, Art. no. 014317.

[45] R. J. Warzoha et al., "Applications and impacts of nanoscale thermal transport in electronics packaging," *J. Electron. Packag.*, vol. 143, no. 2, Jun. 2021, Art. no. 020804.

[46] A. Manoi, J. W. Pomeroy, N. Killat, and M. Kuball, "Benchmarking of thermal boundary resistance in AlGaN/GaN HEMTs on SiC substrates: Implications of the nucleation layer microstructure," *IEEE Electron Device Lett.*, vol. 31, no. 12, pp. 1395–1397, Dec. 2010.

[47] J. Cho, E. Bozorg-Grayeli, D. H. Altman, M. Asheghi, and K. E. Goodson, "Low thermal resistances at GaN–SiC interfaces for HEMT technology," *IEEE Electron Device Lett.*, vol. 33, no. 3, pp. 378–380, Mar. 2012.

[48] F. Mu et al., "High thermal boundary conductance across bonded heterogeneous GaN–SiC interfaces," *ACS Appl. Mater. Interfaces*, vol. 11, no. 36, pp. 33428–33434, 2019.

[49] Y.-C. Hua and B.-Y. Cao, "A two-sensor 3ω-2ω method for thermal boundary resistance measurement," *J. Appl. Phys.*, vol. 129, no. 12, Mar. 2021, Art. no. 125107.

[50] Y. Zhou, J.-Y. Yang, L. Cheng, and M. Hu, "Strong anharmonic phonon scattering induced giant reduction of thermal conductivity in PbTe nanotwin boundary," *Phys. Rev. B, Condens. Matter*, vol. 97, no. 8, Feb. 2018, Art. no. 085304.

[51] Y. Hu, Y. Shen, and H. Bao, "Ultra-efficient and parameter-free computation of submicron thermal transport with phonon Boltzmann transport equation," *Fundam. Res.*, Jun. 2022, doi: 10.1016/j.fmre.2022.06.007.

[52] Y. Xu, L. Yang, and Y. Zhou, "The interfacial thermal conductance spectrum in nonequilibrium molecular dynamics simulations considering anharmonicity, asymmetry and quantum effects," *Phys. Chem. Chem. Phys.*, vol. 24, no. 39, pp. 24503–24513, 2022.

[53] Y. Zhou and M. Hu, "Full quantification of frequency-dependent interfacial thermal conductance contributed by two- and three-phonon scattering processes from nonequilibrium molecular dynamics simulations," *Phys. Rev. B, Condens. Matter*, vol. 95, no. 11, Mar. 2017, Art. no. 115313.

[54] E. Pop, R. W. Dutton, and K. E. Goodson, "Monte Carlo simulation of Joule heating in bulk and strained silicon," *Appl. Phys. Lett.*, vol. 86, no. 8, Feb. 2005, Art. no. 082101.

[55] Y.-C. Hua and B.-Y. Cao, "The effective thermal conductivity of ballistic–diffusive heat conduction in nanostructures with internal heat source," *Int. J. Heat Mass Trans.*, vol. 92, pp. 995–1003, Jan. 2016.